Swiss Light Source upgrade lattice design

Andreas Streun, Masamitsu Aiba, Michael Böge, Ciro Calzolaio, Michael Ehrlichman, Marco Negrazus, Bernard Riemann, and Vjeran Vrankovic

Paul Scherrer Institut, CH-5232 Villigen PSI, Switzerland

(Received 27 April 2023; accepted 7 August 2023; published 1 September 2023)

Following the spectacular success of the third-generation light source over the past decades, a few new-generation light sources based on the multibend achromat (MBA) scheme have come into operation. Other such facilities are also under construction while existing ones are being upgraded. Likewise, the Swiss Light Source, which has been in operation for more than 20 years at the Paul Scherrer Institute, is to be upgraded with the present storage ring being replaced by an MBA low-emittance ring. A natural emittance of 158 pm at a beam energy of 2.7 GeV is achieved for a storage ring of comparatively short circumference, 288 m, providing a gross straight section of 83.6 m. The objectives of the upgrade were met under tight constraints by the application of two novel concepts: the introduction of both a longitudinal gradient and a reverse bend into the unit cell and pushing the superperiodicity to the number of arcs, effectively with "pseudosymmetry." A detailed account of the MBA design and its expected performance is presented and the experience gained is highlighted with the aim to facilitate next-generation light source lattice design.

DOI: 10.1103/PhysRevAccelBeams.26.091601

I. INTRODUCTION

The entire light source community is moving forward to the next generation, where photon beam performance is drastically improved. The new facilities are based on storage rings exploiting the multibend achromat (MBA) lattice [1–3]. MAX IV [4,5], commissioned in August 2015, was the first machine of this kind. ESRF-EBS [6,7] and Sirius [8,9] followed, both achieving first stored beams in December 2019. MBAs comprise multiple bending magnets, with the dispersion function closed (zero) outside the arc, leaving ideal spaces for insertion devices. The storage rings of these facilities are 7-BA or 5-BA whereas those of the third-generation light sources are typically double-BA (DBA) or triple-BA (TBA). Many more MBA storage rings are under construction or in the design phase. These include ALS-U [10], APS-U [11], Diamond II [12], Elettra 2.0 [13], HEPS [14], PETRA IV [15], SOLEIL II [16], etc. (see Fig. 1).

The electron beam emittance in the storage ring, a critical parameter in determining the photon beam spectral brightness, has an approximately inverse-cubic dependence on the number of bending magnets. An MBA-based storage ring consequently offers a natural solution when aiming for electron beam emittance improvements from the present nanometer regime to the picometer regime. Applying such a simple scaling to a 7-BA can, for example, lead to a factor of 40 improvement in emittance when compared to the traditional DBA. There are, however, other issues with MBA that need to be considered (see, e.g., [17]): (i) The increased number of bending magnets per arc leads to a highly compact lattice that limits the available space for other magnets and accelerator components. (ii) The beam should be properly focused at each bending magnet, requiring strong quadrupole magnets in locations where the distance between bending magnets is short. (iii) Strong sextupole magnets are consequently required to compensate for the chromaticity of the resulting strongly focused optics with low beta and low dispersion functions, thereby rendering the lattice highly nonlinear. (iv) Such strong magnets necessitate small magnet bore radii, which in turn lead to a small vacuum chamber aperture making it difficult to reach vacuum pressure specifications due to the limited conductance.

With the experience accumulated over the past decades designing and operating third-generation light sources, the accelerator community is on a good footing to tackle these important issues. Moreover, the significant advances made in nonevaporable getter (NEG) coating [18,19] in recent years mitigate the vacuum pressure problem, making the MBA storage ring, from the engineering aspect, technically feasible.

To ensure that the Paul Scherrer Institute (PSI) remains competitive in the new era of next-generation light sources, the Swiss Light Source (SLS) is to be upgraded. Here, we present the novel SLS upgrade design in detail.

The document is organized as follows: Section II highlights the objectives of the upgrade together with the constraints that define the boundary conditions of our design. Section III describes the lattice design in detail, while the performance of the storage ring is presented in Sec. IV. The iterations in the lattice design are elaborated in Sec. V. Finally, we summarize our conclusions in Sec. VI.

II. OBJECTIVES OF THE UPGRADE AND CONSTRAINTS

The lattice design was made with the following objectives: (i) Maintaining an SLS beam current of 400 mA and the resulting photon flux. (ii) An increase in brightness in the hard x-ray regime by a factor of 40 or more. (iii) A higher coherent flux for ptychography beamlines. (iv) Extending the hard x-ray range of dipole beamlines to a higher energy ($\geq$60 keV) and higher photon flux for soft and tender x-ray (spectroscopy) beamlines. (v) Maintaining the performance of the present SLS in the VUV range ($\approx$20 eV).

A green-field facility was not viable due to financial limitations. The existing infrastructure would therefore be preserved, thereby imposing the following constraints: (i) The new MBA ring is to replace the existing TBA ring, following closely the geometric footprint of the existing storage ring in order to avoid significant modifications to the tunnel and minimize the shifts of photon-beam source points. The circumference of the ring is then limited to about 288 m. (ii) The existing injector complex is to be reused and compatibility with the storage ring, with respect to top-up operation, maintained. (iii) A beam lifetime comparable to that of the present SLS, about 10 h, is to be maintained.

The preservation of the injector complex and the accelerator tunnel were crucial in keeping the so-called dark time (the period corresponding to the absence of synchrotron light) acceptably short, about 18 months.

These objectives and tight constraints, combined with the various MBA issues discussed in Sec. I, in themselves make the design of a new lattice a most difficult and challenging task. Moreover, the maximum magnetic field gradients must also be taken into account. These depend on the beam pipe radius, a key parameter for beam impedance and instabilities. It is, however, impractical to predict an adequate aperture at the onset of the design since the lattice is required for the development of an impedance model and the evaluation of the instability thresholds. Nevertheless, based on our knowledge of accelerator physics and technology, a beam pipe radius of 10 mm was adopted in the initial stage.

This consequently sets a practical limit on the quadrupole and sextupole gradients to $\approx$100 T/m, and $\approx$5000 T/m^2, respectively. Even with such strong magnets, however, it proved difficult to achieve the objectives for the given circumference. A decision was taken to make use of permanent magnets as in Sirius and ESRF-EBS. In our case, all dipole magnets and combined-function magnets, i.e., dipole plus quadrupole, are permanent-magnet based (see Sec. III) [20]. Although the gain in the magnetic field was not significant, their use released precious space that would otherwise have been taken by the electromagnet coils. The limit for the combined-function magnets could not be definitively determined partly due to a lack of practical experience with this type of magnet. The magnet parameters were revisited as described in Sec. V.

The space between magnets is an important parameter in the mechanical integration. For electromagnets, space was reserved at both ends for the coils, amounting to 35, 25, and 15 mm for quadrupoles, sextupoles, and octupoles, respectively.

In addition, a minimal space of 10 mm was reserved between neighboring magnets. The minimum yoke-to-yoke distance was then 25 mm for the pairs of the permanent magnet dipoles (combined function) and the octupoles. This is discussed further in Sec. V.

III. LATTICE DESIGN

The lattice design procedure is presented here in detail. Table I first summarizes the lattice parameters determined from this study. A natural beam emittance of 158 pm at a beam energy of 2.7 GeV is achieved for a comparatively short circumference of 288 m while providing a gross straight section of 83.6 m.

TABLE I. Storage ring parameters. Values with insertion devices are given in parentheses. The natural emittance, for example, is 158 pm/135 pm with/without insertion devices.

Parameters	SLS today	SLS upgrade
Lattice type	TBA	7-BA
Number of arcs	12	12
Circumference (m)	288	288
Gross straight length (m)	79.9	83.6
Total bending angle (deg)	374.69	430.08
Working point Q_x/Q_y	20.43/8.74	39.37/15.22
Momentum compaction factor, first/second order (10^{-4})	6.04/36.3	1.05/7.94
Natural chromaticity ξ_x/ξ_y	$-67.3/-21.0$	$-99.0/-33.4$
Vertical emittance (pm)	$\approx$10	10
Chromaticity in operation	5	1.0–1.5
Energy (GeV)	2.411	2.700
Natural emittance (pm)	5630	158 (135)
Energy spread (10^{-3})	0.88	1.16 (1.04)
Radiation loss per turn (keV)	549	688 (915)
Damping partition $J_x/J_y/J_s$	1.0/1.0/2.0	1.83/1.0/1.17
Damping time $\tau_x/\tau_y/\tau_s$ (ms)	8.65/8.67/4.34	4.14/7.58/6.47
Beam current (mA)	400	400
Maximum rf voltage (MV)	2.6	2.2
Harmonic number	480	480
Number of bunches	390–420	450
Beam lifetime (h)	$\approx$10	$\approx$9

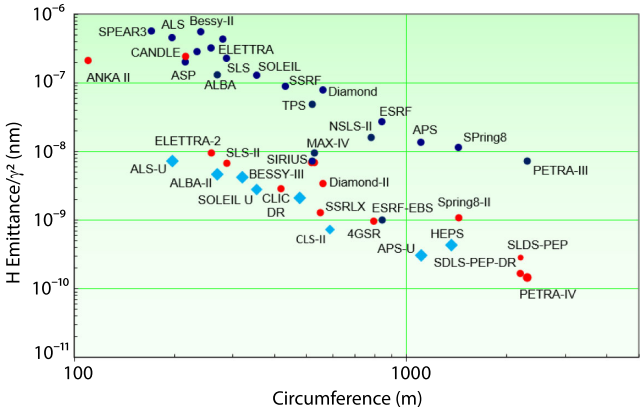

FIG. 1. Natural emittance of various light source facilities. Operating facilities are in dark blue, new projects in red and cyan. Facilities marked in red/cyan have off-axis/on-axis injection (or similar variants). Figure by courtesy of R. Bartolini, dated July 2022.

The study of the beam collective effect is itself extensive and outside the scope of the present paper. It is, however, described in [21], from where it is concluded that collective effects will not prevent operation with a beam current of 400 mA even though the momentum compaction factor of the new storage ring is significantly lower.

Figure 1 shows the natural emittances of existing and new light source facilities. The emittance is normalized to the square of beam energy and plotted as a function of circumference on a logarithmic scale. It is evident that new facilities (including MAX-IV, ESRF-EBS, and Sirius) with MBA storage ring provide a significantly lower emittance. The upgraded SLS will be one of the first of such new generation facilities.

Figure 2 shows a snapshot of one sector of the storage ring and illustrates the compactness of the lattice.

The lattice design described in this section was performed using various accelerator codes, namely, OPA [22], ELEGANT [23], MAD-X [24], Bmad [25] and TRACY [26,27].

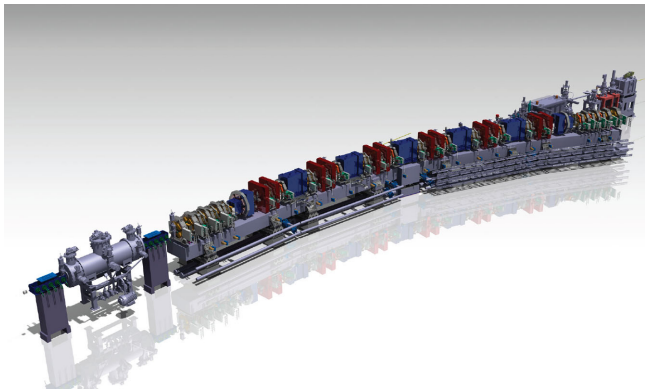

FIG. 2. One sector of the storage ring from a three-dimensional virtual model. The number of magnets per arc is more than 100.

A. Linear optics design

1. Unit cell and periodic MBA lattice

The horizontal phase advance of the theoretical minimum emittance cell (TME cell) [28] becomes too high when the emittance is fully minimized. This type of cell is consequently applied with relaxed parameters, meaning the TME cannot be realized. A novel concept, the LGB-RB cell [29,30], which combines the longitudinal gradient bend (LGB) [31–33] and the reverse bend (RB) [34–36], was therefore employed to overcome this difficulty. Figure 3 compares the LGB-RB cell to a typical TME type cell. We find that the emittance in the LGB-RB cell is lower than that of the TME cell by approximately a factor of 4.

The negative bending of the RB is gainfully employed as a tuning knob by which a negative angular dispersion may be applied. This serves to lower the dispersion function at the LGB center through the rather large horizontal phase advance of the low emittance cell. Low dispersion suppresses quantum excitation of the emittance even at the high peak field of the LGB.

Such manipulation of the dispersion is not possible with a TME type cell because the knob (quadrupole) changes both the dispersion function and the beta function, resulting in too large a horizontal phase advance. The reverse bend,

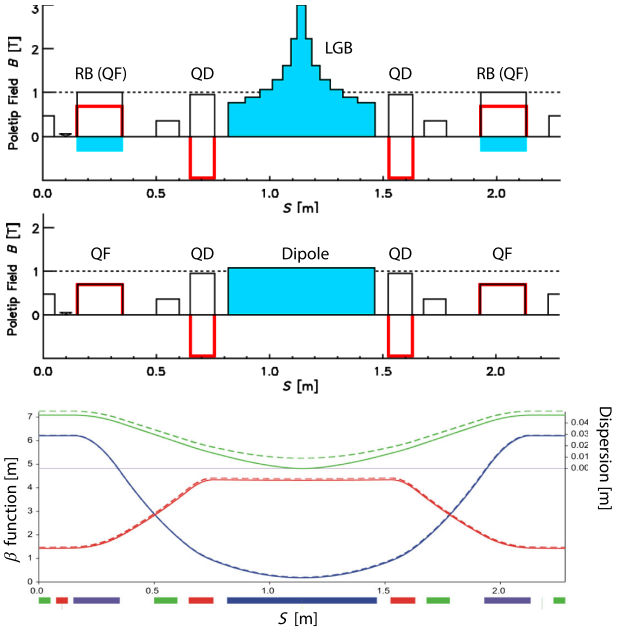

FIG. 3. LBG-RB and TME type cells. Top and middle plots show the magnet configuration of the LGB-RB and TME type cells, respectively. The pole tip field is at a radius of 13 mm for a 2.4-GeV electron beam. The corresponding optical functions are shown in the bottom plot with solid/dashed lines indicating the LGB-RB/TME type cell. The net bending angle is 5 deg in both cases, with common cell tunes of 0.429 and 0.143 in the horizontal and vertical planes, respectively. The natural emittance of the LGB-RB/TME type cells is 103 pm/427 pm, respectively, for a 2.4-GeV electron beam.

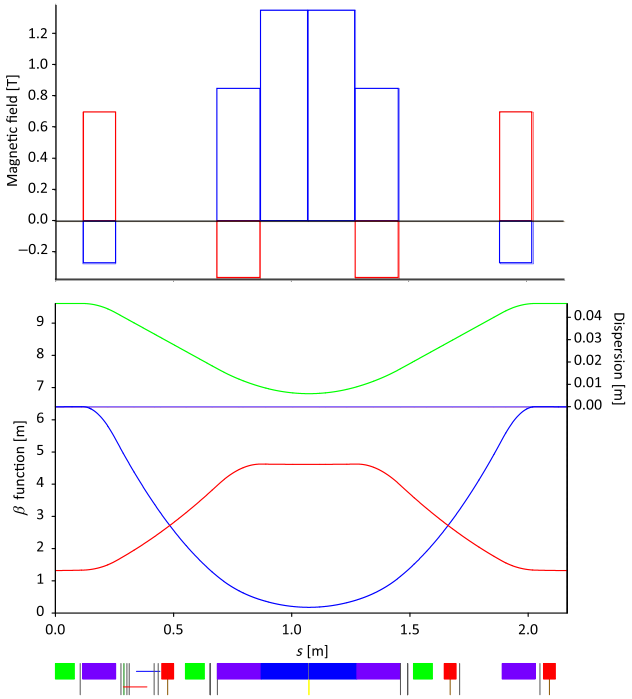

FIG. 4. Magnetic field and optical functions of a unit cell. In the upper plot, blue and red lines represent the dipole and quadrupole fields, respectively, at a reference radius of 9 mm (the inner vacuum pipe radius). In the lower plot, blue and red lines represent the horizontal and vertical beta functions, respectively, while light green shows the dispersion function. At the bottom of the figure, blue and purple boxes represent the dipole and combined-function magnets (dipole and quadrupole), respectively. These magnets determine the linear optics of the unit cell. Green boxes represent sextupole magnets for chromaticity corrections, while red boxes are the quadrupoles for tuning and optics corrections. This color code for the optical function and magnet configuration also applies to similar plots throughout the paper.

however, controls the dispersion function while remaining largely transparent to the beta function.

The beam emittances in six dimensions follow the Robinson's sum rule [37]. This allows the horizontal emittance to be lowered at the expense of a larger energy spread. In practice, this is achieved by introducing transverse gradients into bending magnets (defocusing in normal bending and/or focusing in RB). Transverse gradients are, therefore, incorporated into the LGB-RB cell. The resulting damping partition numbers are listed in Table I.

Figure 4 shows the actual unit cell of the SLS upgrade lattice. The LGB is implemented in a simplified manner with three magnets: a pure dipole magnet with no gradient in the center, with weaker dipoles, which include a transverse gradient, attached at either end. The emittance is minimized when the LGB field profile has its highest peak in the center and varies smoothly with the dispersion function. This configuration provides, however, an acceptable compromise between the emittance and magnet complexity.

The core of the MBA arc consists of unit cells with a dispersion suppressor (DS) attached at either end of the arc. The DS, in essence, is a modified half-unit cell in our case. A minor modification is necessary because of the nonzero dispersion at the LGB center. The length of the DS half cell, the transverse field gradient in both RB and LGB, and the bending angle of those magnets are adjusted to suppress the dispersion outside the MBA. While these knobs alone are sufficient to fully suppress the dispersion, a further knob from the unit cell is nevertheless used to facilitate the process (Fig. 5).

The lattice has matching sections to wrap up the MBA arc and to optimize the beta function along the straight section. Figure 5 illustrates a sector with five unit cells and two half cells (7-BA).

The length of the unit cell is 2.165 m, which is much shorter than the distance between the dipoles of the TBA of the present storage ring, which is about 5 m. To accommodate all essential components, the RBs and the LGB in Fig. 4 are permanent magnets, which require less longitudinal space. The strong gradients of these magnets focus the beam horizontally at the LGB (or every short cell).

The absolute natural chromaticity is about 50% higher than that of the present TBA lattice (Table I). Far stronger sextupoles are required to counteract the poor chromaticity correction efficiency due to the low beta and dispersion functions (Fig. 5). Therefore, it is important to formulate a control of the nonlinear optics already at the stage of the linear optics design. Unit cell phase advances are determined such that they cancel most resonance driving terms. The values selected are $3/7$ and $1/7$ in units of 2π in the horizontal and vertical planes, respectively [38].

2. *Pseudosymmetry*

The present storage ring has a threefold geometrical symmetry, with straight sections of three different lengths, which are referred to as short, middle, and long straights. The requirement to comply with the given accelerator tunnel consequently dictates a maximum superperiodicity of 3. A novel concept, named "pseudosymmetry," is therefore introduced to increase the superperiodicity to the number of arcs, which is 12. For an on-energy particle, only the phase advance, in terms of nonlinear optics, needs to be considered for any part of the ring without a nonlinear element. In other words, a variation of beta functions over such a linear section is transparent to the nonlinear optics provided the phase advances are kept constant.

Following this idea, the optics of the straight sections were designed with common phase advances. Figure 6 shows the optical functions of the entire ring. A pseudosymmetry is realized in spite of the beta functions themselves not possessing a 12-fold symmetry.

The chromaticity correction sextupoles are located at the dispersive section, i.e., within the achromat. In addition, three more sextupoles are installed in each matching section.

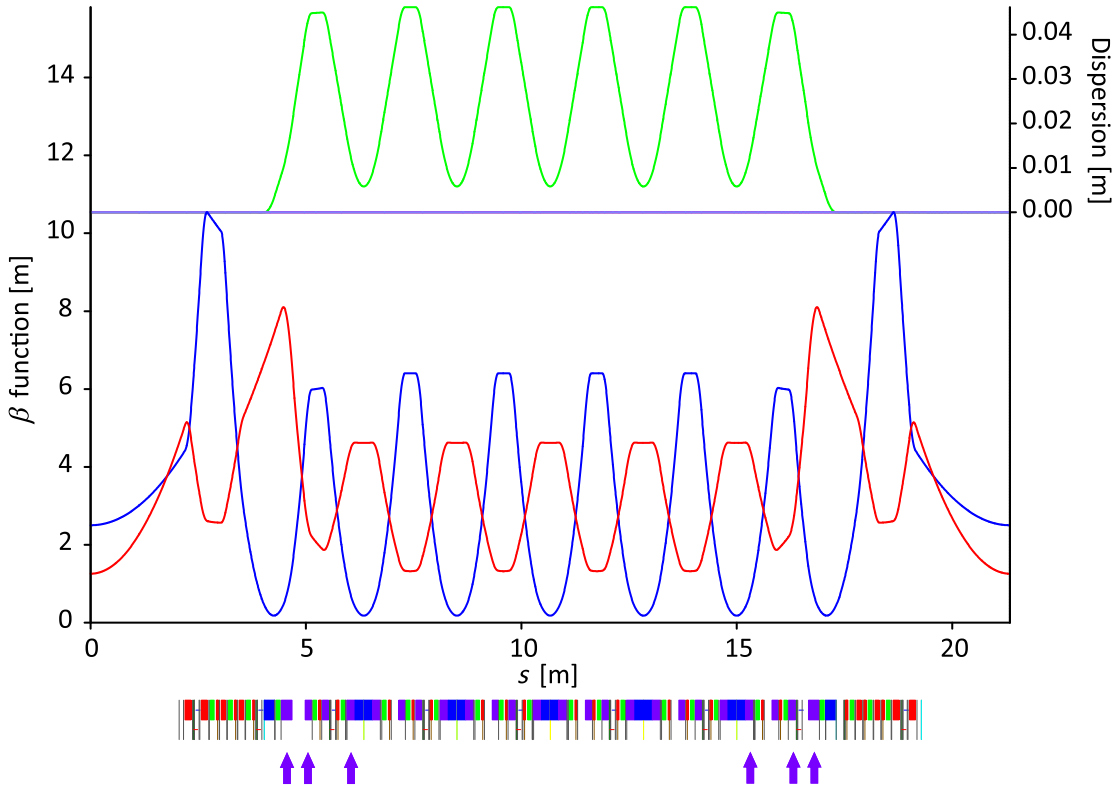

FIG. 5. Optical functions of a 7-BA sector with a short straight section. The arrows at the bottom point to the locations of the combined-function magnets, whose gradients are adjusted to suppress the dispersion outside the MBA.

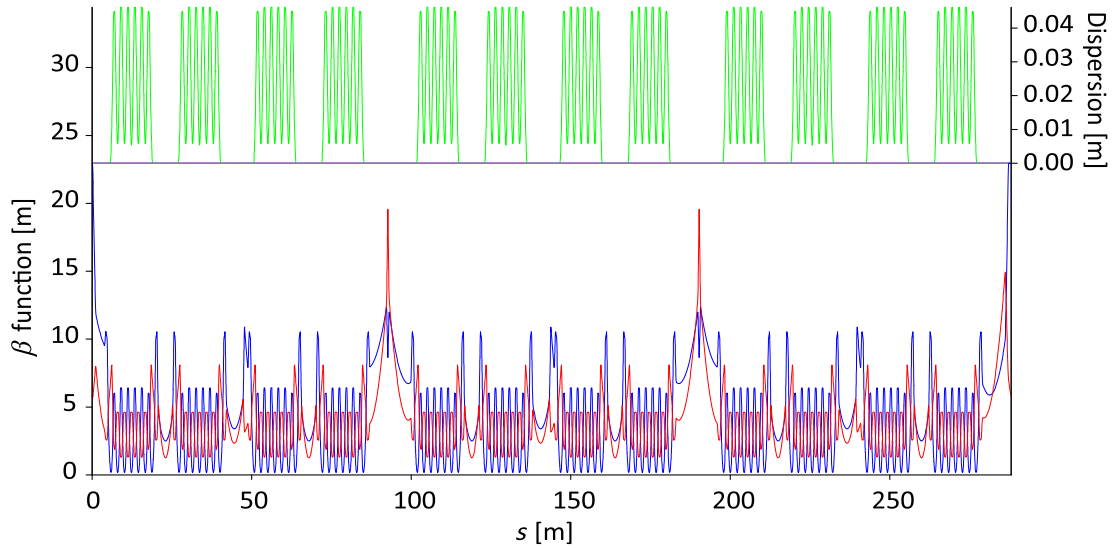

FIG. 6. Optical functions of the storage ring.

The latter sextupoles are referred to as harmonic sextupoles while the former as chromatic sextupole.

The matching section is then divided into two parts. The first is composed of two quadrupoles and three harmonic sextupoles, while the second, which faces the straight section, consists of two quadrupoles only. A few additional quadrupoles are inserted into the middle and long straight sections. The straight section together with two second parts of the matching section (upstream and downstream of the straight section) defines the linear section. The horizontal and vertical phase advances of the 12 linear sections are adjusted to the same values. In this configuration, the beta functions are identical for all 12 sectors except for these linear sections. Identical sextupole settings are

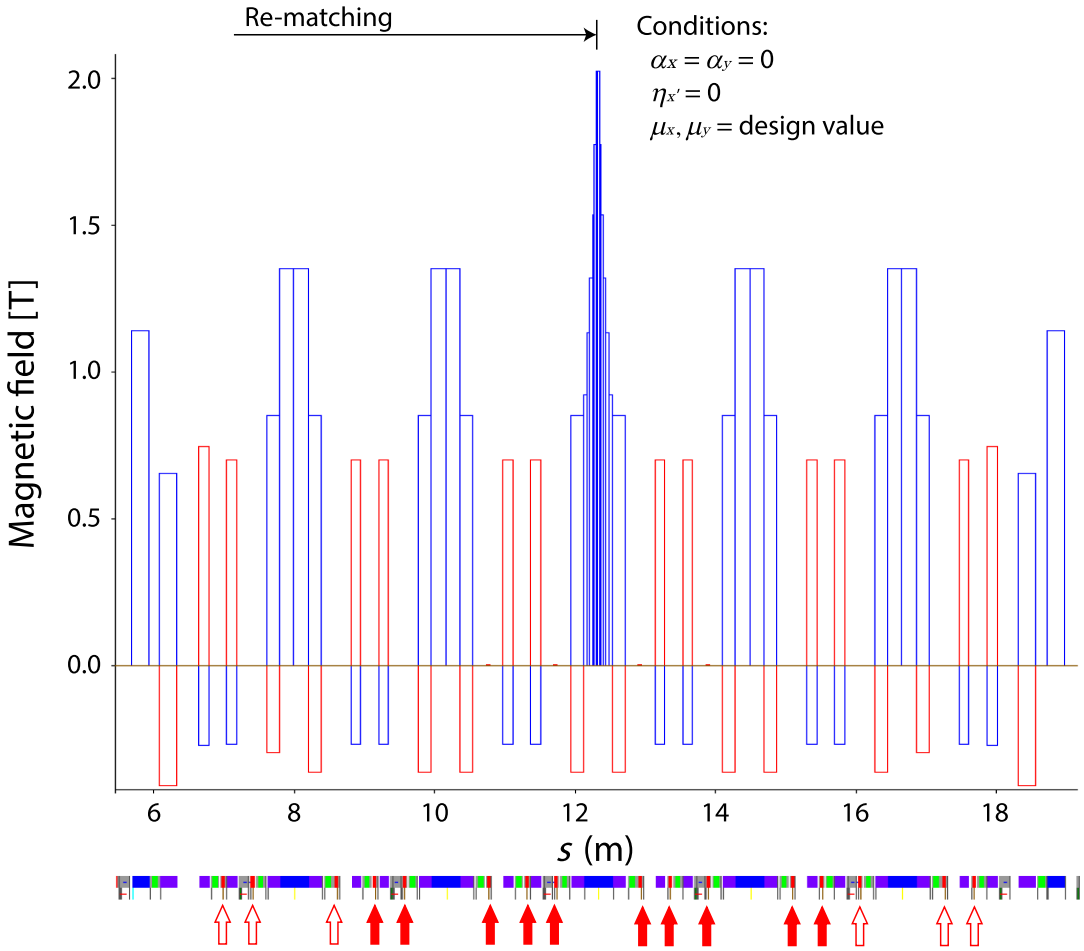

FIG. 7. Field profile of dipole (blue) and quadrupole (red) components at a reference radius of 9 mm. The dipole in the center is exchanged by a superbend of 2.1 T peak field, modeled with short dipole slices. Arrows at the bottom of the figure indicate the location of the quadrupole correctors. The filled arrows point to the subset used for the optics rematching with superbend.

applied to all sectors. The superperiodicity of the storage ring is then equal to the number of arcs for the on-energy particle. The effectiveness of pseudosymmetry is examined in Appendix A.

Pseudosymmetry imposes a common phase advance. The beta functions along the straight section, however, remain flexible to some extent. For instance, in the long straight section used for injection, the horizontal beta function at the injection septum is increased to 23 m in order to magnify the dynamic aperture. The injection is further discussed in Sec. III D.

3. Plug-in superbend

Superbend magnets with high peak fields [21] are integrated into the arcs to provide very hard x-rays, in accordance with the objectives of the upgrade. Four permanent magnet superbends, with a peak field of 2.1 T, are initially planned. Two of these will later be replaced by superconducting superbends with peak fields of ≈5 T that are tunable.

A feature of the lattice is that superbend magnets can be readily "plugged-in." Only the central dipole of the LGB is to be exchanged by a superbend. The superbend magnet can therefore be transverse gradient free, thereby significantly simplifying its design.

The linear optics is slightly perturbed by the superbends but the lattice is capable of compensating for this perturbation by means of the quadrupole correctors (see Sec. III C). The superbend is to be located in the center of the arc, and five quadrupole correctors on each side are used to rematch the optical functions (Fig. 7).

The optics perturbation after rematching is hardly noticeable. It is, nevertheless, sufficient to excite a nonsystematic third integer resonance, $3Q_x = 118$. The design horizontal tune was 39.35, and we slightly moved it to 39.37 to avoid the $3Q_x = 118$ resonance.

B. Nonlinear optics

The inefficiency of chromaticity corrections and the resulting lattice nonlinearity have already been emphasized.

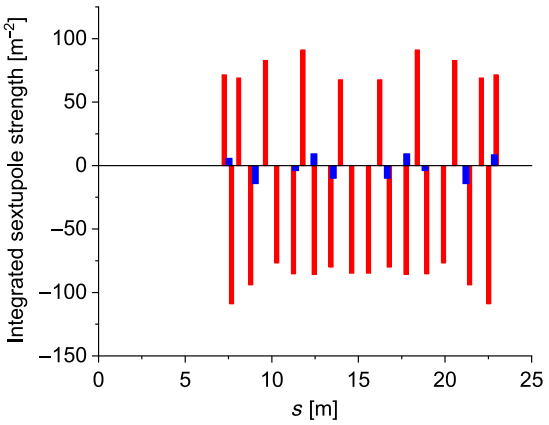

FIG. 8. Sextupole strength of the present (blue) and upgraded (red) storage rings. The strength is integrated over each magnet and normalized to the magnetic rigidity of the beam.

Figure 8 illustrates this by displaying the integrated sextupole strengths for the present and future storage rings.

Although the phase advances of the unit cell are carefully selected, the cancelation of sextupole kicks is imperfect. The choice of $3/7$ and $1/7$ is ideal for seven unit cells. The MBA arc has six cells including modified DS half cells. The matching sections, which partly include optical functions similar to that of the unit cell, are used to compensate for the one missing cell. Moreover, not all resonance driving terms are canceled even for the ideal case of seven identical cells.

This deficiency can be corrected by using the harmonic sextupoles and by simultaneously varying the chromatic sextupoles from cell to cell. Furthermore, a number of octupoles located at dispersive and nondispersive locations allow the amplitude-dependent tune shifts (ADTSs) and higher-order chromaticity to be manipulated to some extent. They are referred to as chromatic and harmonic octupoles, analogous to the sextupoles. Harmonic octupoles are located only in the first part of the matching sections to maintain the pseudosymmetry. A total of 24 sextupoles and 22 octupoles are finally incorporated into each sector. They are positioned such that a mirror symmetry is established around the center of each sector and paired with respect to this symmetry. The number of knobs available to regulate the nonlinear optics is thus 12 sextupole pairs and 11 octupole pairs per sector.

Determining the optimum set of sextupole and octupole strengths is a complex problem. The targets of the optimization are as follows: (i) chromaticity in both transverse planes (exact values); (ii) amplitude dependent tune shifts (minimization); (iii) higher-order chromaticity (minimization); (iv) dynamic aperture (maximization); and (v) momentum aperture (maximization).

The optimization is performed in two steps. The first step is to minimize the resonance driving terms, ADTSs, and chromatic tune shifts. The optimization algorithm implemented in the OPA code is used. It considers the resonance driving terms up to the fourth order, ADTSs at the given betatron amplitudes, and the chromatic tune shift up to the third order. We emphasize that the dynamic aperture is not included in this optimization loop. The second step of the optimization is based on numerical tracking. Starting with a lattice already optimized in the first step of the procedure, the sextupole and octupole knobs are further adjusted empirically to improve the target values. ADTSs, chromatic tune shifts, and the dynamic apertures (on-energy and off-energy apertures) are computed and directly included in the optimization. The linear chromaticity is set to zero in both planes such that only the higher-order chromatic tune shifts are visible. The dynamic aperture is typically improved by 10%–20% in this second step.

Once the optimization is complete, the chromaticity can be set to its operation point, in the range from 1.0 to 1.5, without significantly degrading the dynamic aperture.

Optimizations using MOGA and other algorithms were also applied (see [39–41] and references therein). These approaches arrived at comparable solutions [41].

Figure 9 shows the dynamic aperture, ADTS, and chromatic tune shifts of the optimized lattice.

C. Optics tunability and correction capability

Although the quadrupole magnets in the matching sections are electromagnets, the MBA linear optics is fully based on permanent magnets with no tuning capability [42]. In order to introduce essential lattice tunability and correction capability, each octupole incorporates normal and skew quadrupole corrector functionalities by means of additional windings.

The quadrupole correctors together with the quadrupoles in the matching section allow the betatron-tune working point to be varied in both planes in a range of ± 0.5 and beyond, depending on the direction in the tune space. The selected working point (Table I), however, was the optimum choice when considering the nonlinear optics [43].

Quadrupole correctors are used for linear optics correction, beam-based alignment (see Sec. IV), and optics rematching for the superbend. Skew quadrupole correctors serve for coupling correction and adjustment of the vertical emittance, which is to be set to 10 pm for user operation. The large number of skew quadrupole correctors (22 per sector, as many as the octupoles) makes it possible to introduce betatron coupling and vertical dispersion along the arc while suppressing them along the straight sections. Adverse effects on the photon beam performance from coupling correlations or a dispersive beam size increase are therefore not to be expected. The horizontal and vertical dispersion functions for the 10-pm setting are shown in Fig. 10.

The dipole orbit correctors are stand-alone devices, each paired with a beam position monitor (BPM). The storage

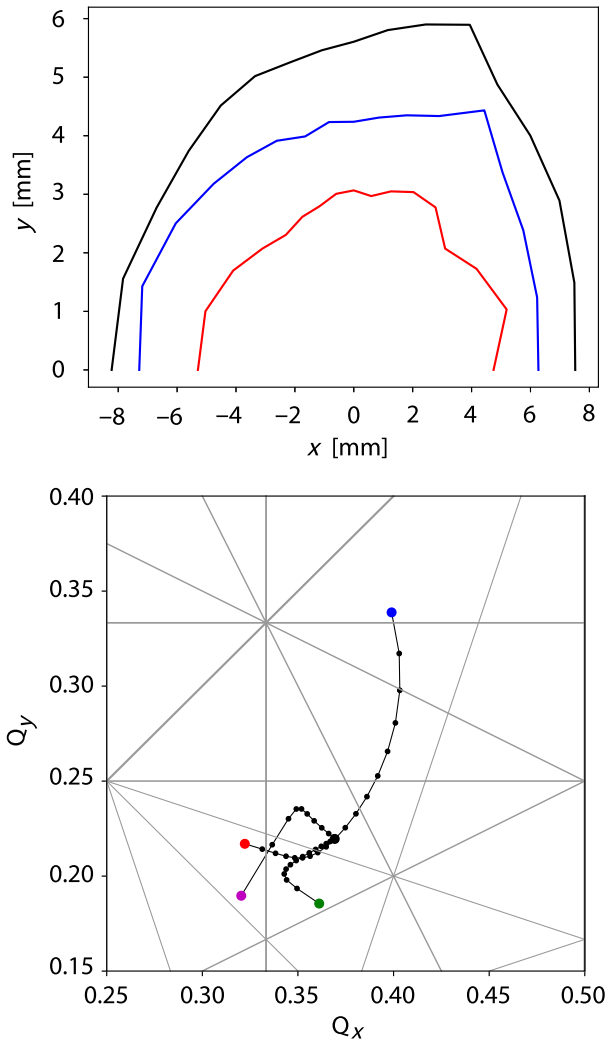

FIG. 9. Dynamic aperture (top) and tune footprint (bottom) of the ideal, error-free lattice. The dynamic aperture is computed at the location of the thin septum (see Sec. III D) for −3% (red), 0% (black), and +3% (blue) energy deviations. The branches of the tune footprint are ADTSs and chromatic tune shifts. Green and purple branches are ADTSs along horizontal and vertical oscillation amplitude, blue and red branches are chromatic tune shifts up to +4.5% and −4.5% energy deviation. The chromaticity is set to +1.0 in both planes.

ring is equipped with 115 such correctors in each plane and a matching number of BPMs dedicated to orbit correction. The ideal layout would place these every 90 deg (or less) in phase advance. This desirable condition, however, cannot be fulfilled for our horizontal tune of 39.37; this is further discussed in Sec IV. Within the unit cell, the corrector and BPM unit is installed in one of two available spaces between LGB and RB. The remaining space (downstream of LGB) is required for the synchrotron radiation absorber, consequently limiting the number of correctors and BPMs.

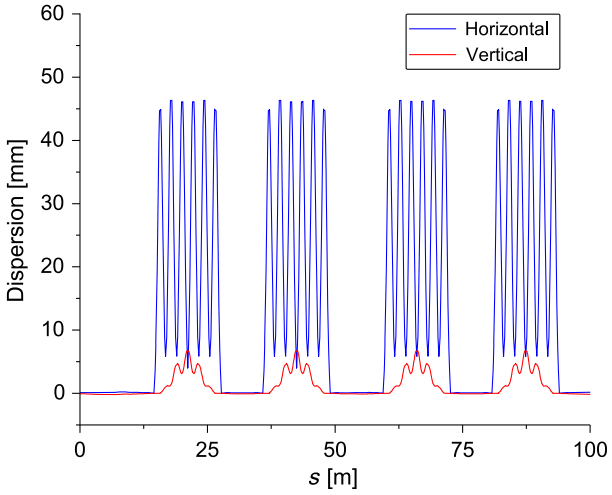

FIG. 10. Horizontal and vertical dispersion functions along one third of the storage ring. Vertical dispersion bumps are generated with skew quadrupoles to set the vertical emittance to 10 pm.

D. Injection

Two injection schemes are to be implemented: the conventional kicker-bump injection, as in the present SLS, and "aperture sharing" using a short-pulse kicker.

The rather limited available aperture makes it difficult to apply the conventional injection scheme. To achieve it, two important parameters need to be refined, the injection beam emittance and the septum blade thickness. The injection beam emittance can be lowered through an emittance exchange in the injector booster [44], as has been experimentally proven [45]. The horizontal emittance of the SLS booster is rather low, 12.5 nm at 2.7 GeV [46]. A full exchange can therefore be applied (within the limitation arising from radiation damping) since the vertical emittance after the exchange still fits the storage ring aperture. The horizontal emittance after the exchange will be 2 nm or less. (The emittance exchange experiment was performed at 2.4-GeV beam energy, which is the nominal SLS beam energy, while we need to adopt it for the 2.7-GeV beam energy of the SLS upgrade.) A septum blade of only 1-mm thickness can be realized by dividing the injection septum into a thick and a thin part, as demonstrated by the ALS [47].

These improvements make it possible to apply the conventional injection scheme together with the high beta function at the location of the septum. Figure 11 shows the beta function along the injection straight.

Four additional quadrupoles in the injection straight section realize pseudosymmetry and regulate the beta function. Two of the four are placed between the thick and the thin septum, requiring their apertures to be sufficiently large to allow the injection beam to pass through. It is planned to reuse the quadrupoles of the present SLS storage ring (30-mm bore radius). This serves as an illustration for how much larger the aperture of

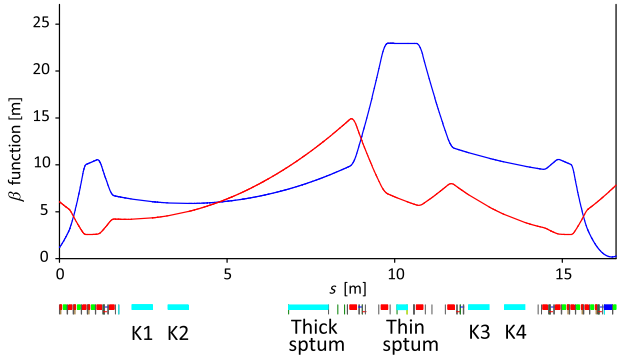

FIG. 11. Beta functions along the injection straight. Light blue boxes at the bottom indicate the locations of the injection devices, i.e., four bump kickers and thick and thin septum.

the present storage ring is, compared to that of the new storage ring.

The second injection scheme, "aperture sharing," is realized with a short-pulse kicker, to be installed in the straight section after one MBA arc [48]. The injected beam passes through the first arc with a large betatron oscillation amplitude and is inflected into the aperture by the short-pulse kicker. The stored beam bunches are simultaneously deflected by the kicker but remain within the aperture provided the deflection is sufficiently small. This condition is fulfilled thanks to both the lower injection beam emittance and the thin septum.

The number of bunches disturbed by the kicker depends on its pulse length. A short-pulse kicker (under development) limits the number of disturbed bunches to 15 out of 450 stored, achieving a quasitransparent injection. In the future, the pulse may be shortened down to the nanosecond level, which would enable almost fully transparent injection with only a few bunches disturbed [49].

Figure 12 shows the beams in the horizontal phase space at the location of the thin septum, as obtained from numerical tracking simulations.

Table II summarizes the lengths and deflection angles of the injection hardware. Technical details of the injection hardware are found in Ref. [21]. It is planned to reuse the existing SLS injection kicker, while the thin septum will be newly manufactured. Two options have been under consideration for the thick septum: a pulsed septum and a permanent-magnet septum following the study of Ref. [50]. The latter has the advantage of minimizing the disturbance to the stored beam. We recently decided to adopt the permanent-magnet septum, and its design is to be finalized soon.

E. Magnet parameters

Through the lattice design described above, we arrive at the magnet parameters summarized in Table III.

When the vertical magnetic field component, B_y, of an ideal multipole magnet on the median plane is represented as a function of horizontal position, x,

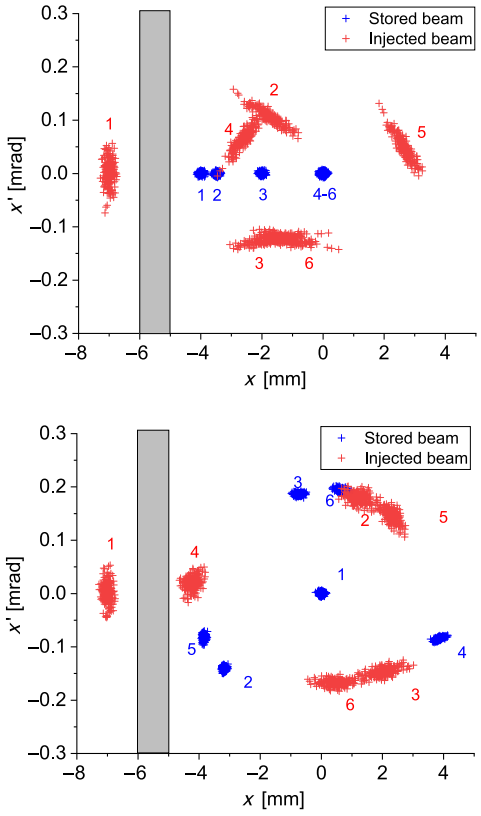

FIG. 12. Stored and injected beams in horizontal phase space at the location of the thin septum for kicker-bump injection (upper plot) and aperture sharing (lower plot). Tracking simulation is performed using the ELEGANT code [23] with the ideal lattice. A bunch of 200 particles is tracked for each injection scheme. The numbers in the plots indicate the number of turns, following the injection.

$$B_y = B_n x^{n-1}, \tag{1}$$

the sextupole ($n = 3$)/octupole ($n = 4$) gradient in Table III corresponds to B_3/B_4.

F. Radiofrequency bucket

All straight sections are filled with insertion devices to generate photon beams and/or with other essential accelerator components. Space was allocated for four 500-MHz

TABLE II. Injection hardware, lengths, and deflection angles. The length of the thick septum is that of a pulsed septum. (A permanent magnet septum will be shorter.) The bump kickers are singly powered, i.e., four pulses are used.

Device	Length	Deflection angle
Thick septum	1.5 m	7 deg
Thin septum	0.3 m	13.5 mrad
Bump kicker	4×0.6 m	−2.6–2.4 mrad
Short-pulse kicker	2×0.8 m	≈300 μrad each

TABLE III. Magnet parameters. The field gradient is given as an absolute value. "CF" stands for combined function (dipole and quadrupole), "DS" for dispersion suppressor, and "MS" for matching section. The field gradients of the electromagnets and bending angles of the orbit correctors are the values at maximum power supply currents. The parameters are the ones of the hard-edge optics model.

Magnet type	Length (mm)	Field gradient and/or strength	Bending angle (deg)
Permanent magnet			
Dipole of LGB	405.0	1.35 T	3.48
CF of LGB, defocusing	185.0	40.6 T/m, 0.85 T	1.00
Superbend	405.0	2.1 T or 5 T peak	3.48
RB, focusing	140.0	77.6 T/m, 0.27 T	−0.24
Dipole of LGB in DS	242.5	1.14 T	1.76
CF of LGB in DS, defocusing	240.0	45.7 T/m, 0.65 T	1.00
RB in DS, focusing	150.0	82.8 T/m, 0.25 T	−0.26
Electromagnet			
MS quadrupoles	170.0	93.0 T/m	0
	210.0	98.0 T/m	0
Large bore quad.	200.0	23.2 T/m	0
Chromatic sextupole	80.0	5850 T/m^2	0
Sextupole in DS	90.0	5850 T/m^2	0
Harmonic sextupole	90.0	5850 T/m^2	0
Octupole	50.0	63000 T/m^3	0
Orbit corrector, H/V	50.0	2.36 mT/1.57 mT	0.0344/0.0229
Quad corrector	50.0	5.6 T/m	0
Skew quad corrector	50.0	5.6 T/m	0

rf cavities with higher-order mode dampers in one long straight section, and two-third harmonic cavities (1.5 GHz) in another. The former are normal conducting active cavities while the latter are superconducting passive cavities. With four 500-MHz cavities, a peak voltage of 2.2 MV can be provided. It is planned to operate the storage ring with an rf voltage between 1.44 and 1.72 MV, depending on which insertion devices are in use. An alternative operational scenario is to keep the voltage constant at around 1.72 MV. The technical details of the rf cavities are described in [21].

The third harmonic cavities, when properly tuned, flatten the rf bucket potential at the synchronous phase and prolong the stored beam bunches longitudinally. The harmonic number of the fundamental rf is 480, with 450 buckets to be filled. The gap of 30 buckets serves to suppress ion instabilities [21]. It is expected that the average bunch lengthening factor is about 2.6 with beam loading in the passive cavities [51].

Figure 13 shows the rf bucket in longitudinal phase space. A flattened potential is evident. The bucket is asymmetric, i.e., the momentum acceptance spans from −6.0% to +4.5% [52].

IV. PERFORMANCE

A. Lattice performance

Machine imperfections such as magnet misalignments and field errors are inevitable. The dynamic and momentum apertures may be degraded, leading to a shorter beam lifetime. The impact of machine imperfections must therefore be evaluated in order to validate the feasibility of the designed lattice. Numerical tracking simulations are widely used for such a performance evaluation. We used TRACY for the tracking presented in this section.

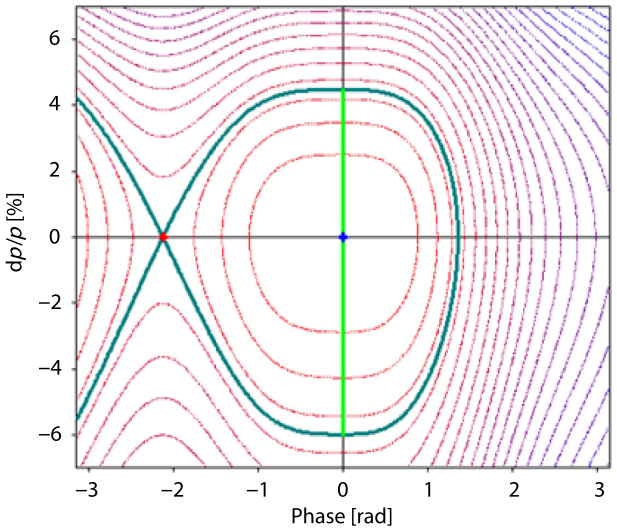

FIG. 13. Radiofrequency bucket in longitudinal phase space (dark green curve). Blue and red dots indicate stable and unstable fixed points, respectively. The light-green vertical line corresponds to the bucket height. The third harmonic cavities are turned on, whereas the insertion devices are turned off.

TABLE IV. Machine imperfections applied to the performance evaluation. Misalignments and field errors are given by a Gaussian distribution truncated at two standard deviations. The girder-to-girder misalignment value is that after adjusting the girder position based on beam measurements. All allowed multipoles up to 20-poles are considered for the electromagnet multipole error. Magnets in the lattice are in close proximity to one another. The octupole field is therefore excited in the sextupole adjacent to the RB, although it is not an allowed pole. Normal and skew quadrupole correctors excite higher multipoles in the octupole by an amount that depends on the current in the additional windings.

Parameter	Value
Misalignment	
Element-to-element	30 μm rms
Girder center	60 μm rms
Girder-to-girder	20 μm rms
BPM offset	300 μm rms
Magnet rotation	300 μrad rms
BPM rotation	10 mrad rms
Field error	0.2% rms
Multipole error	
Permanent magnet	Up to 12 poles
Quadrupole	12 and 20 poles
Sextupole	18 poles
Sext. next to RB	8 poles in addition
Octupole	12 and 20 poles

Realistic lattices were generated by applying random magnet misalignments and field errors. Furthermore, higher multipole errors, quantified through three-dimensional field computation, are also included in the evaluation. The imperfections applied are summarized in Table IV.

The tracking study revealed multipole errors to be nondetrimental. This is attributed to the fact that the nonlinearity of the lattice is dominated by the strong sextupoles and that the fields of higher multipoles are not significant for betatron oscillations, whose amplitudes are limited by the relatively small dynamic aperture.

The multipole error model is to be developed further with the inclusion of field measurement results, although this is not expected to have a significant impact on the lattice performance. The influence of insertion devices is the subject of a separate study [21]. It will be integrated into the error model of Table IV.

The magnet misalignments, although small, can greatly affect the lattice performance, mainly because of the strong sextupoles positioned in the lattice, as shown in Fig. 8. When the closed orbit does not correspond to the sextupole axis horizontally, a feed-down quadrupole component is introduced, leading to a beta beating. Likewise, a vertical orbit offset along the sextupole introduces a skew quadrupole component, which leads to a transverse coupling. The quadrupolar field errors are also important sources of beta beating.

The performance evaluation is carried out after first applying an orbit correction, a BPM beam-based alignment (BBA), a linear optics correction, and a coupling correction. By applying these corrections, we assess whether the correction capability described in Sec. III C is adequate to compensate for machine imperfections.

Figure 14 shows a closed orbit after applying a BPM BBA and an orbit correction. It is a typical example generated from one of the performance evaluations using random seeds. The BPMs are aligned with respect to the closest quadrupole or quadrupole corrector. The closed orbit after the orbit correction is therefore nonzero at the BPMs since the quadrupoles are misaligned with respect to the ideal orbit ($x = y = 0$). Large BPM offsets can be corrected with a BBA. The statistical measurement error can be at the 1 μm level [53] but there may be systematic errors that degrade the BBA accuracy, such as the error in the calibration of the quadrupole axes with respect to the

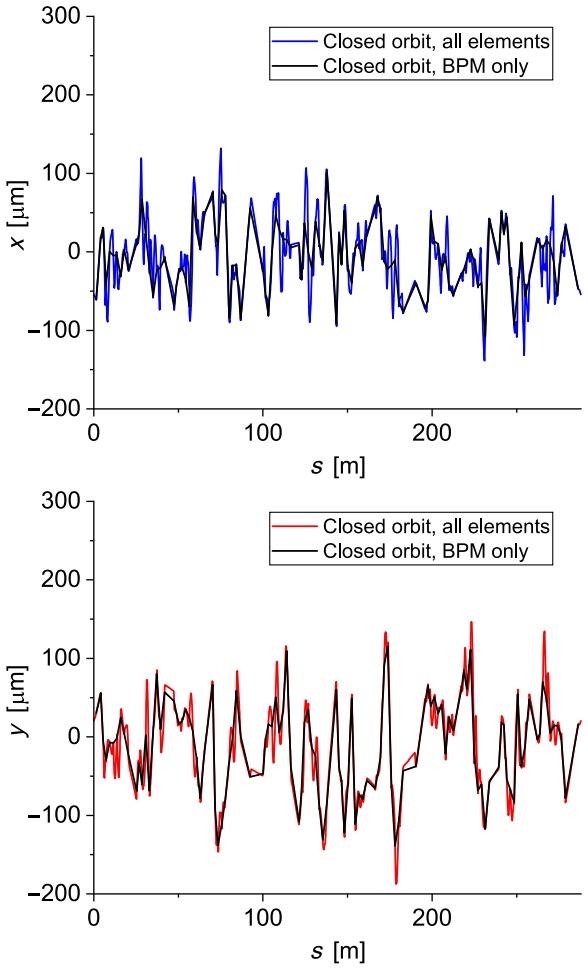

FIG. 14. Example of a closed orbit after BPM BBA and orbit correction in the horizontal (upper plot) and vertical (lower plot) plane. The black and colored (blue, red) curves correspond to sampling at the location of the BPMs only, and at all accelerator components, respectively.

reference marker used for mechanical survey alignment. To include the impact of these errors, the BPMs are randomly shifted with respect to the quadrupole axes by 10 μm rms. The BBA in the new storage ring is described in detail in Ref. [53].

The curves shown in Fig. 14 are from the closed orbit data sampled at the locations of the BPMs (black) and all accelerator components (blue/red). An orbit correction can be applied such that the BPM readings converge to zero. The curves displayed in Fig. 14 show a deviation due to the (randomly generated) misalignment, with the peak deviation reaching ≈100 μm. Such a large peak appears more often in the horizontal plane because of the higher betatron tune in that plane.

Having implemented the BBA and orbit corrections, the linear optics and coupling corrections are applied next. The correction based on an orbit response matrix, originally implemented in LOCO [54], is adopted in the evaluation. The measurement of the orbit response matrix is simulated for 50 random seeds, and the simulated matrix is used to find an optimum setting for quadrupoles and skew quadrupoles. The horizontal and vertical dispersion corrections are also included in the simulation. The results are summarized in Fig. 15. The beta beating is typically corrected to 1% or below and the vertical dispersion to below 1 mm. The horizontal dispersion correction is not as effective as that for the vertical plane (Fig. 15) but is sufficient to maintain the lattice performance. The increase in beam size due to the residual dispersion is marginal. Figure 16 shows the dynamic aperture for these seeds after the corrections.

Finally, the Touschek lifetime was computed for the same set of random seeds, see Fig. 17, employing lattices that were well uncoupled after coupling corrections (emittance ratio 5×10^{-3} or smaller). The local momentum aperture is computed along the ring as an input for the liefetime calculation (Fig. 18). The vertical emittances were very small in these lattices, and an artificial emittance of 10 pm was assumed for the computation.

As discussed in Sec. III C, skew quadrupole correctors are to be used to control the vertical emittance. This will lead to a lifetime shorter by about 1 h because Touschek scattering within the vertical dispersion bump results in a betatron oscillation in the vertical plane, which may be intercepted by the undulator gaps. An interesting alternative option to adjusting the vertical emittance is the application of white or pink noise to the beam, which does not degrade the lifetime.

Taking other factors into account, namely, Coulomb scattering (90 h for 10^{-9} mbar of carbon monoxide), Bremsstrahlung (35 h), and bunch prolongation resulting from the third harmonic cavity, a net beam lifetime of 9 h is foreseen, comparable to that under present SLS operating conditions. With a vertical emittance of 10 pm, the influence of intrabeam scattering is found to be marginal.

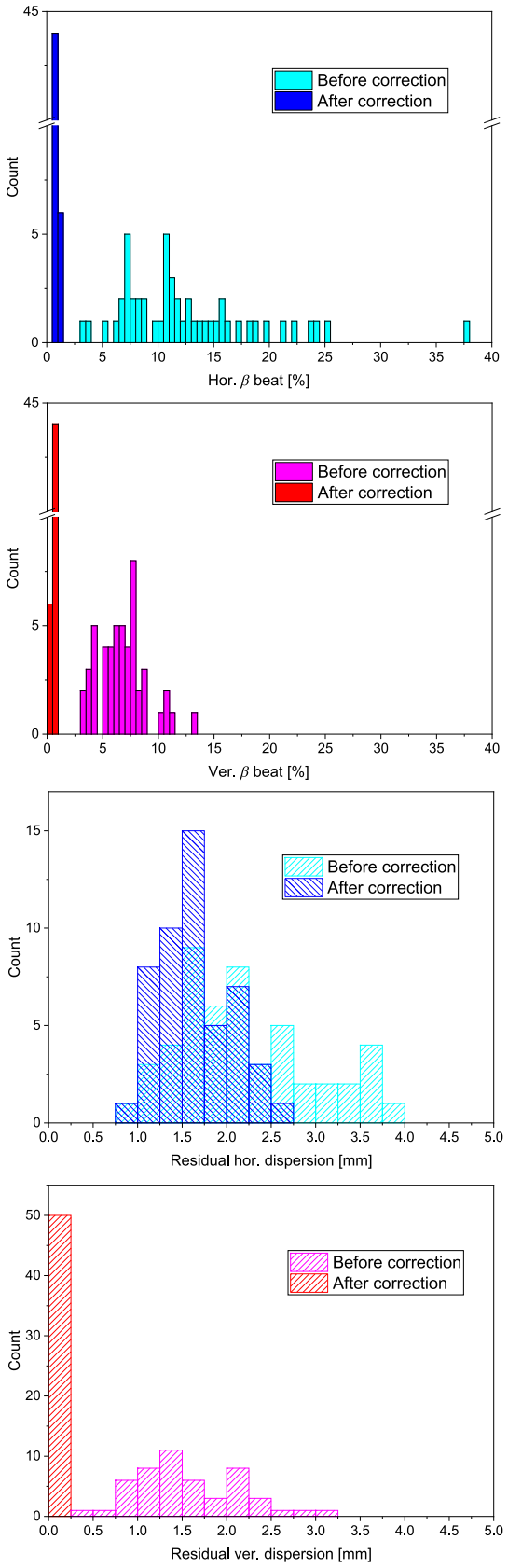

FIG. 15. Beta beat and residual dispersion before and after correction. From top to bottom, horizontal beta beat, vertical beta beat, horizontal dispersion, and vertical dispersion.

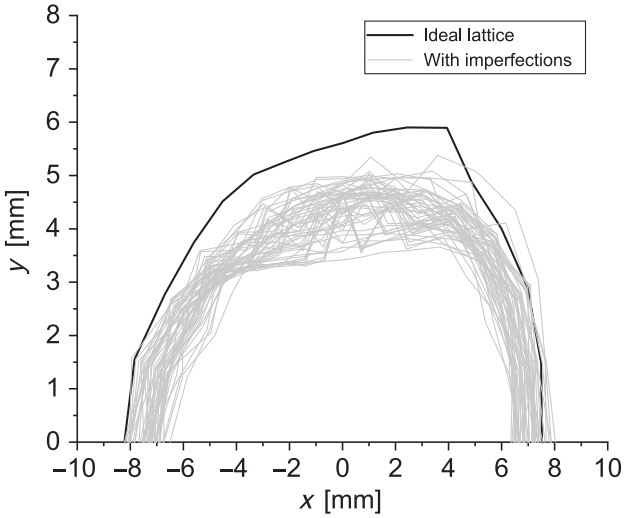

FIG. 16. On-momentum dynamic aperture after applying linear optics and coupling corrections.

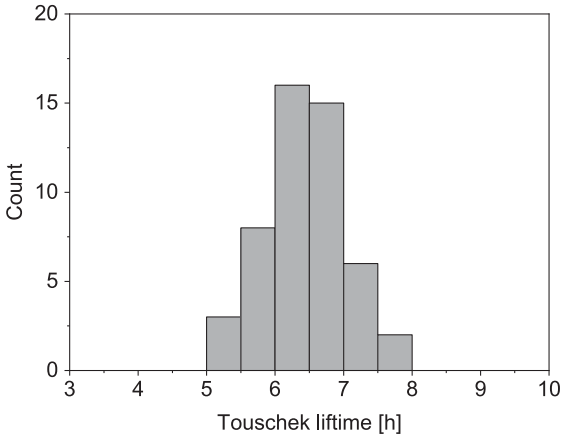

FIG. 17. Touschek lifetime without a third harmonic cavity. The average over 50 random seeds is 6.42 h, to be compared to 7.10 h for the ideal lattice case.

The performance of the lattice is evaluated after applying the corrections using dipole, normal quadrupole, and skew quadrupole correctors. The sextupoles and octupoles can act as correction knobs for nonlinear optics. This correction is not yet fully explored in our lattice but will be conducted with the actual machine.

Another important objective of the machine imperfection study was to confirm, through numerical simulations, that the entire commissioning process could be executed without undue difficulty [55].

B. Photon beam performance

The spectral brightness depends on various parameters but is determined to a large degree by the electron-beam emittance. The optical functions at the source point are,

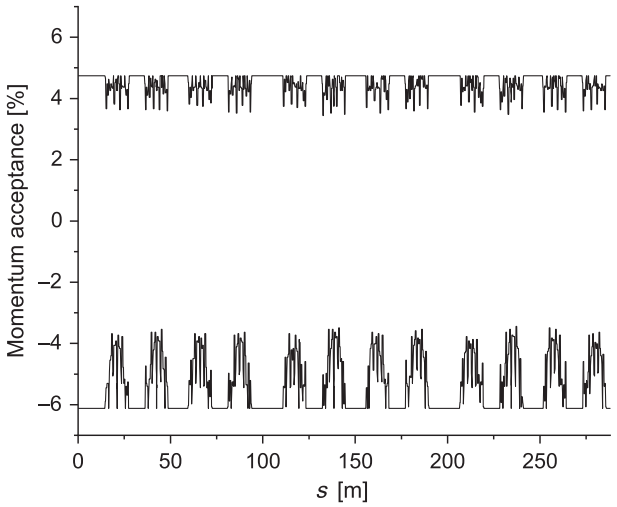

FIG. 18. Local momentum aperture of the ideal lattice. The corresponding Touschek lifetime, without harmonic cavity, is 7.10 h.

however, equally important. The optimum beta function at the photon source location (see, e.g., [56]) is given by

$$\beta_{x,y} = \frac{L}{2\pi}, \tag{2}$$

where L is the length of the insertion device. The lengths of insertion devices are in a range from 0.98 to 3.3 m, which corresponds to an optimum beta function from 0.16 to 0.53 m. It is difficult to achieve such low beta: in the middle of the short straight section, the beta functions are 2.50 and 1.26 m in the horizontal and vertical plane, respectively. A recent paper stated that the optimum beta near the diffraction limit may rather be L/π [57]. This, however, remains outside our possibility.

One of the objectives is to improve the spectral brightness in the hard x-ray regime by at least a factor of 40 with respect to that of the present SLS. The actual gain in the natural emittance is comparable to this requirement. In the short sections of the present SLS, however, the beta functions at the location of the insertion devices are closer to the optimum values: 1.38 and 1.02 m in the horizontal and vertical planes, respectively. This shortcoming of the beta functions is, however, compensated for by new insertion devices, with shorter undulator periods and/or higher fields, in conjunction with the increased beam energy. Figure 19 shows the overall performance of the upgraded machine.

V. DESIGN REVISIONS TO CONSOLIDATE FEASIBILITY

A. Momentum compaction factor

In spite of the robust design strategy described in Sec. III, many versions were developed and discarded before

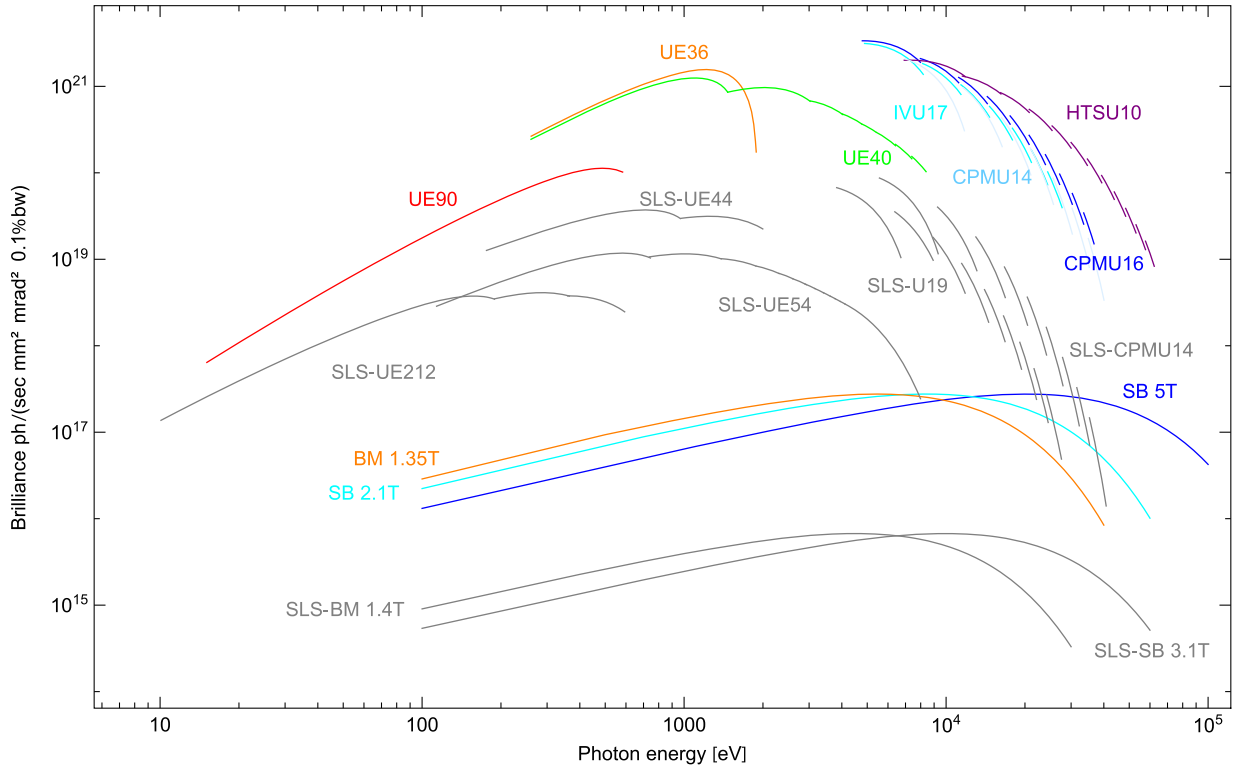

FIG. 19. Photon beam spectral brightness. Gray curves (with prefix "SLS") represent the present SLS for comparison. Figure by courtesy of T. Schmidt.

finalizing the lattice. In the early design stage, as described in the conceptual design report (CDR) [29], lattices with negative momentum compaction factor were considered. In the unit cell with reverse bending magnets, the dispersion function at the LGB can be varied independently of the beta function. This feature allowed us to reach the minimum emittance by pushing down the dispersion function, even to a negative value at the LGB. The lattice with negative momentum compaction factor, however, was abandoned for two reasons. First, a beam experiment performed at UVSOR in the past showed that the microwave instability threshold was much lower with negative momentum compaction factor [58]. Second, the need for stronger reverse and normal bending magnets started to reach the technical limits of magnet feasibility. A lattice design with a positive momentum compaction factor was therefore initiated. The beam pipe radius was adjusted from 10 to 9 mm during this revision.

A positive consequence of these changes was the possibility to increase the beam energy from 2.4 to 2.7 GeV due to the corresponding relaxation of the magnet specification. The undulator harmonics shift to a higher photon energy with the flux being increased in accordance with the increase in beam energy.

B. Photon beam extraction

At a later stage, it was recognized that the apertures of the photon beam extraction channels were limited. The photon beam generated in the straight section diverges after the first bending magnet, which, in essence, is a half LGB (combined-function magnet attached to only one side) in the dispersion suppressor. The sextupole and the octupole downstream proved to be the bottleneck. A solution was provided by a modified dispersion suppressor, whereby the half LGB was divided into two to provide space for the sextupole to be inserted in-between, and the octupole removed. This modification was also applied to the dispersion suppressor at the other end of the MBA arc so as to maintain symmetry. The nonlinear optics was well reoptimized in this new configuration with one octupole pair less per arc. Even with the above change, we had to abandon extracting low-energy photons below 20 eV.

Photon beam extraction is a common issue for the new generation of light sources, where the beam pipe radius is small. It is crucial to investigate this issue as soon as a first working lattice is obtained.

C. Orbit corrector

The present SLS storage ring is equipped with multifunction sextupoles, which incorporate horizontal and vertical orbit correctors, and a skew quadrupole through additional coil windings. The initial study assumed orbit correctors within the sextupole. It transpired, however, that the decapole field could reach values large enough to degrade the dynamic aperture. Moreover, the sextupole

operation point was either close to or within the saturation regime and thus the linearity of the orbit corrector field could not be guaranteed. These were the primary arguments for choosing stand-alone orbit correctors.

Furthermore, space for the orbit corrector was available within the unit cell between RB and LGB. In the matching section, space is required between quadrupoles to properly control the optics. It is shared between multipole magnets and the stand-alone orbit correctors.

D. Magnet cross-talk

Magnets that are too close together affect each other's field. We observed that such interaction is prone to be significant when the permanent magnet is involved. While the allocated space between magnets was sufficient to enable their mechanical integration, the three-dimensional finite-element-mesh (FEM) field simulations uncovered considerable "cross-talk" between neighboring magnets. The minimum yoke-to-yoke distance of 25 mm between the octupole and the combined-function magnet (RB) was particularly problematic. The octupole return yoke absorbs the field of the RB, preventing the RB to reach its design gradient.

On the other hand, the maximum sextupole gradient of the designed magnet (5850 T/m^2) was higher than initially required (5200 T/m^2). Moreover, the requirement came from the harmonic sextupoles while the chromatic sextupoles were well below the maximum gradient even after the beam energy increase. The chromatic sextupole was consequently shortened by 10 mm, and the distance between the octupole and the RB was increased correspondingly. The actual octupole magnet yoke length of 44 mm is shorter than the original value of 50 mm in the lattice. This difference is a direct outcome of the octupole magnet optimization, where the effective magnet length is adjusted, rather than any cross-talk mitigation. The yoke-to-yoke distance was nevertheless increased to about 40 mm.

Another change driven by the cross-talk issue was the distance between the RB and the dipole orbit correctors. The problem was solved in a similar manner to that of the octupole case. The space taken from the focusing sextupole was allocated to the octupole problem while the space taken from the defocusing sextupole was allocated to the corrector problem. A magnetic shield to intercept the field from the RB to the corrector was introduced for further mitigation.

We position the magnets such that the cross-talk effects are compensated. A strong effect was observed between the dipole at either end of the MBA and the neighboring sextupole. The fringe field of the dipole was attenuated by the sextupole, and thus the vertex point of the dipole was shifted. The dipole magnet was shifted longitudinally to compensate for the vertex shift. A further strong cross-talk effect was an interference between the reverse bend and the neighboring sextupole. As seen in Fig. 8, the strength of chromaticity correction sextupoles varies from magnet to magnet. It was necessary to adjust the gradients of the reverse bends, depending on the neighboring sextupole magnet strength in order to recover the design linear optics. We have managed to adjust the positions and gradients, for most magnets so far, such that the cross-talk effects become negligible, in terms of the beam orbit and linear optics, compared with the other machine imperfections (Table IV).

The investigation of cross-talk effects is an ongoing process since it relies on time-consuming FEM simulations. While the study is yet to be completed, it is nevertheless sufficiently advanced to verify the feasibility of the lattice with its design changes. A detailed account of the cross-talk study is foreseen for the near future.

VI. CONCLUSION

The lattice design of the Swiss Light Source upgrade proved to be extraordinarily challenging given the stringent constraints imposed by the boundary conditions of the existing accelerator tunnel. Nevertheless, the goals of the upgrade have been accomplished. The key to its success is the novel concept applied to the lattice, namely, the LGB-RB cell and pseudosymmetry. A natural emittance of 158 pm (without insertion devices), at a beam energy of 2.7 GeV for a given circumference of 288 m, is achieved. The lattice performance has been examined with critical attention. The dynamic aperture, including inevitable machine imperfections, is sufficiently large to provide for a high injection efficiency and a beam lifetime suitably long for user operation. The obtained photon beam performance fulfills the objectives.

Simultaneously achieving low emittance and long lifetime is a difficult task, if not impossible. Other upgrade projects have introduced an on-axis injection scheme [11,59] to relax the dynamic aperture requirement for injection, thereby allowing a lower emittance to be reached at the expense of a shorter beam lifetime. In this case, the correlation of momentum aperture, which determines Touschek lifetime, to dynamic aperture is the reason for the shorter lifetime. The lifetime can be prolonged (or recovered) by applying a round-beam scheme but the spectral brightness is then lowered. We managed to fulfill the lifetime requirement while preserving compatibility with the off-axis injection schemes.

The experience gained in the lattice design procedure, with all its revisions and iterations, has also been presented and may serve as an aid to future new-generation light-source lattice designers.

As a final remark, reference is made to the so-called hybrid MBA [60] lattice concept, which was also considered as an alternative approach. The rationale for favoring an MBA lattice comprised of periodic unit cells over a hybrid MBA is discussed in Appendix B.

ACKNOWLEDGMENTS

The design study has benefitted from numerous interactions with the various hardware groups at PSI, making the final lattice feasible both from a beam dynamics and an engineering perspective. We would like to thank Hans Braun for valuable discussions and comments, Simona Bettoni for investigating the influence of insertion devices, Johan Bengtsson for optimizing the nonlinear optics for the CDR lattice, and Pantaleo Raimondi for help with the hybrid MBA lattice alternative. Finally, we are grateful to Jan Chrin and Thomas Schietinger for proofreading the manuscript.

APPENDIX A: EFFECTIVENESS OF PSEUDOSYMMETRY

To examine the effectiveness of pseudosymmetry, we break the symmetry of the designed lattice. The three different straight sections, namely, long (L), middle (M), and short (S), are arranged in a pattern of L-S-M-S that repeats 3 times. Within the above string, the horizontal phase advance of the first S-straight is increased while it is decreased in the second one, such that the betatron-tune working point does not move. When such a phase variation is applied to one third of the ring (two S straights), the superperiodicity for the on-energy particle will be 1, while it will be 3 when all six S-straight sections are involved.

The dynamic apertures of those modified lattices are computed as shown in Fig. 20. It degrades as soon as the period-one modification is introduced. A phase deviation of up to 0.075 is tolerable in case of the period-three modification. This is attributed to the fact that resonances up to the fifth order that overlap with the tune footprint are not structure resonances for a superperiodicity of 12 nor 3.

The lifetime, however, is less tolerant of pseudosymmetry violation (Fig. 21) because the off-energy beta and dispersion functions are further removed from 12-fold symmetry.

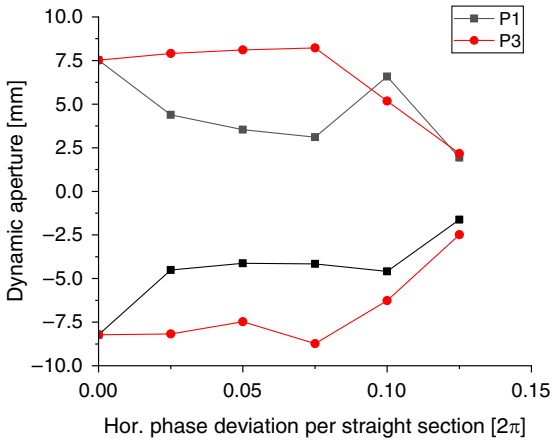

FIG. 20. Dynamic apertures with period-one (P1) and period-three (P3) modifications.

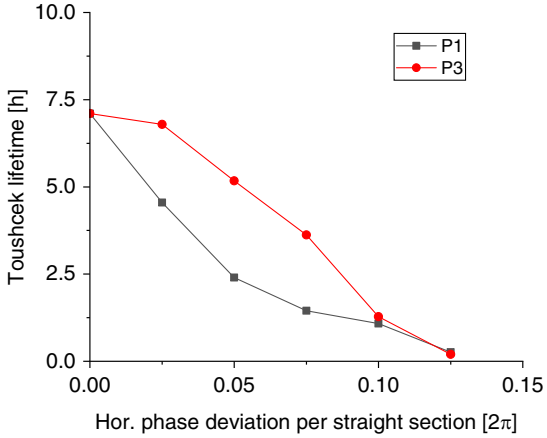

FIG. 21. Touschek lifetime with period-one (P1) and period-three (P3) modifications.

APPENDIX B: CHOICE OF LATTICE FOR THE SWISS LIGHT SOURCE UPGRADE

The MBA lattice with periodic unit cells is well suited for the incorporation of sextupoles and octupoles along the arc, despite limitations in the available space, allowing off-energy optics to be regulated. A machine with low beam energy, $\lesssim 3$ GeV, requires an enlarged momentum aperture to ensure a Touschek lifetime that is suitably long for user operation. A higher energy machine, on the other hand, is able to tolerate a smaller momentum aperture since the energy transfer from the transverse to the longitudinal plane is relatively small.

ESRF-EBS employs the elegantly designed so-called hybrid MBA lattice. The dipole magnets at both ends of the MBA are located some distance away from the central MBA region that comprises very short (nonperiodic) cells. Where chromaticity correction sextupoles are installed in the liberated spaces, the dispersion and the beta functions are enlarged to improve the efficiency of the chromaticity correction. In addition, the phase advances are adjusted such that the condition of a negative unity transformation (see, e.g., [56]) is achieved. Since the sextupole kicks cancel within the MBA arc, a large dynamic aperture is realized even when strong focusing is applied to the central region to minimize the emittance.

The hybrid MBA lattice was considered an alternative for the SLS upgrade. Its attraction lay in the fewer number of magnets, leading to a much simpler mechanical integration. The primary motivation for finally settling on the periodic MBA lattice was the lower emittance that could still be attained under the given constraints [60], especially due to the fixed arc length imposed by the existing tunnel structure. The provision of space for dispersion bumps generally leads to a reduction in the packing factor of dipole magnets.

In the green-field scenario, however, where the arc length can be varied, the central region of the hybrid lattice can be

stretched to accommodate more focusing cells. This approach would make it far simpler to achieve an ultralow emittance when compared to a periodic MBA with >7 bends. Moreover, it has recently been found that the momentum aperture of the hybrid lattice can be improved by symmetrizing the W-function [61] (or by extending the pseudosymmetry concept to off-energy particles). The hybrid MBA lattice therefore remains an attractive option, in particular, for a green-field machine of whatever electron beam energy.

[1] D. Einfeld and M. Plesko, Design of a Diffraction-limited Light Source, *Proc. SPIE 2013, Electron-Beam Sources of High-Brightness Radiation* (1993), https://doi.org/10.1117/12.164802.

[2] W. Joho, P. Marchand, L. Rivkin, and A. Streun, Design of a Swiss Light Source (SLS), in *Proceedings of the 4th European Particle Accelerator Conference, London, England, 1994* (EPS-AG, London, UK, 1994), pp. 627–629.

[3] D. Einfeld, J. Schaper, and M. Plesko, Design of a Diffraction Limited Light Source (DIFL), in *Proceedings of the Particle Accelerator Conference, Dallas, TX, 1995* (IEEE, New York, 1995), pp. 177–179.

[4] MAX IV Detailed Design Report (2010).

[5] P. F. Tavares *et al.*, Commissioning and first-year operational results of the MAXIV 3 GeV ring, J. Synchrotron Radiat. **25**, 1291 (2018).

[6] EBS Storage Ring Technical Report, edited by D. Einfeld (2018).

[7] P. Raimomdi *et al.*, Commissioning of the hybrid multibend achromat lattice at the European Synchrotron Radiation Facility, Phys. Rev. Accel. Beams **24**, 110707 (2021).

[8] Sirius light source: https://lnls.cnpem.br/sirius-en/.

[9] L. Liu, M. B. Alves, F. H. de Sá, A. C. S. Oliveira, and X. R. Resende, Sirius Commissioning results and operation status, in *Proceedings of the 12th International Particle Accelerator Conference, IPAC-2021, Campinas, SP, Brazil* (JACoW, Geneva, Switzerland, 2021), pp. 13–18.

[10] https://als.lbl.gov/als-u/overview/.

[11] Advanced Photon Source Upgrade Project Final Design Report (2019), https://publications.anl.gov/anlpubs/2019/07/153666.pdf.

[12] Diamond-II Technical Design Report, edited by R. P. Walker (2022).

[13] E. Karantzoulis *et al.*, Elettra 2.0 Technical Conceptual Design Report, Elettra–Sincrotrone Trieste Report No. ST/M-17/01, Internal Document (2017).

[14] Y. Jiao *et al.*, The HEPS project, J. Synchrotron Radiat. **25**, 1611 (2018).

[15] PETRAIV Upgrade of PETRA III to the Ultimate 3D X-ray Microscope Conceptual Design Report, edited by C. G. Schroer, R. Röhlsberger, E. Weckert, R. Wanzenberg, I. Agapov, R. Brinkmann, and W. Leemans (2019), https://bib-pubdb1.desy.de/record/426140/files/DESY-PETRAIV-Conceptual-Design-Report.pdf.

[16] Conceptual Design Report Sychrotron SOLEIL Upgrade (2021), https://www.synchrotron-soleil.fr/en/news/conceptual-design-report-soleil-upgrade.

[17] R. Hettel, Challenges in the design of diffraction-limited storage rings, in *Proceedings of 5th International Particle Accelerator Conference, IPAC2014, Dresden, Germany* (JACoW, Geneva, Switzerland, 2014), pp. 7–111.

[18] C. Benvenuti, Non-evaporable getters: From pumping strips to thin film coatings, in *Proceedings of 6th European Particle Accelerator Conference* (1998), pp. 200–204, https://accelconf.web.cern.ch/e98/PAPERS/THZ02A.PDF.

[19] C. Benvenuti *et al.*, A novel route to extreme vacua: The non-evaporable getters thin film coatings, Vacuum **53**, 219 (1999).

[20] Another motivation to utilize the permanent magnet is energy saving. The electricity consumption of the storage-ring magnets will be reduced by ≈60%.

[21] SLS 2.0 Storage Ring Technical Design Report, edited by T. Garvey, PSI Bericht Report No. 21-02, 2021.

[22] Project web site, http://ados.web.psi.ch/opa/.

[23] M. Borland, Elegant: A flexible SDDS-compliant code for accelerator simulation, Advanced Photon Source LS-287 (2000). Project web site: https://ops.aps.anl.gov/elegant.html.

[24] Project web site: http://madx.web.cern.ch/madx/.

[25] Project web site: https://www.classe.cornell.edu/bmad/.

[26] H. Nishimura, TRACY, a tool for accelerator design and analysis, in *Proceedings of 1st European Particle Accelerator Conference, Rome, Italy* (1988), pp. 803–805, https://accelconf.web.cern.ch/e88/PDF/EPAC1988_0803.PDF.

[27] Project web site: https://github.com/jbengtsson/tracy-3.5/.

[28] L. C. Teng, Minimizing the emittance in designing the lattice of an Electron Storage Ring, Fermilab Report No. FERMILAB/TM-1269, 1984.

[29] SLS-2 Conceptual Design Report, edited by A. Streun, PSI Bericht Report No. 17-03, 2017.

[30] B. Riemann and A. Streun, Low emittance lattice design from first principles: Reverse bending and longitudinal gradient bends, Phys. Rev. Accel. Beams **22**, 021601 (2019).

[31] A. Wrulich, Overview on 3rd generation light sources, in *Proceedings of Workshop on Fourth Generation Light Sources* (Stanford Synchrotron Radiation Laboratory, Stanford, CA, 1992), p. 28.

[32] R. Nagaoka and A. F. Wrulich, Emittance minimisation with longitudinal dipole field variation, Nucl. Instrum. Methods Phys. Res., Sect. A **575**, 292 (2007).

[33] A. Streun and A. Wrulich, Compact low emittance light sources based on longitudinal gradient bending magnets, Nucl. Instrum. Methods Phys. Res., Sect. A **770**, 98 (2015).

[34] K. Steffan, The wiggler storage ring: A device with strong radiation damping and small beam emittance, Deutsches Elektronen-Synchrotron Report No. DESY PET-79/05, 1979).

[35] J. P. Delahaye and J. P. Potier, Reverse bending magnets in a combined-function lattice for the CLIC damping ring, in *Proceedings of the 1989 Particle Accelerator Conference, Chicago, IL* (IEEE, New York, 1989), pp. 1611–1613.

[36] A. Streun, The anti-bend cell for ultralow emittance storage ring lattices, Nucl. Instrum. Methods Phys. Res., Sect. A **737**, 148 (2014).

[37] K. W. Robinson, Radiation effects in circular electron accelerators, Phys. Rev. **111**, 373 (1958).
[38] J. Bengtsson and A. Streun, Robust design strategy for SLS-2, PSI internal note, Report No. SLS2-BJ84-001, 2017.
[39] M. Borland, V. Sajaev, L. Emery, and A. Xiao, Direct methods of optimization of storage ring dynamic and momentum aperture, in *Proceedings of the 23rd Particle Accelerator Conference, Vancouver, Canada* (IEEE, Piscataway, NJ, 2009), pp. 3850–3852.
[40] M. P. Ehrlichman, Genetic algorithm for chromaticity correction in diffraction limited storage rings, Phys. Rev. Accel. Beams **19**, 044001 (2016).
[41] M. Kranjčević, B. Riemann, A. Adelmann, and A. Streun, Multiobjective Optimization of the dynamic aperture using surrogate models based on artificial neural networks, Phys. Rev. Accel. Beams **24**, 014601 (2021).
[42] The dipoles and combined-function magnets are equipped with field moderator plates. However, the setting of the plates can be varied only by hand, and the plates are not meant to tune nor correct the optics. Rather, the purpose of the moderator plates is to adjust the magnetic field before the accelerator installation.
[43] Different working points are to be studied further in the context of the beta functions at the locations of insertion devices.
[44] P. Kuske, Transverse emittance exchange for improved injection efficiency, in *Proceedings of 7th International Particle Accelerator Conference, Busan, Korea* (JACoW, Geneva, Switzerland, 2016), pp. 2027–2031.
[45] J. Kallestrup and M. Aiba, Emittance exchange in Electron Booster Synchrotron by coupling resonance crossing, Phys. Rev. Accel. Beams **23**, 020701 (2020).
[46] W. Joho, M. Muñoz, and A. Streun, The SLS booster synchrotron, Nucl. Instrum. Methods Phys. Res., Sect. A **562**, 1 (2006).
[47] D. Shuman *et al.*, Stray field reduction of ALS Eddy current septum magnets, in *Proceedings of the 21st Particle Accelerator Conference, Knoxville, TN, 2005* (IEEE, Piscataway, NJ, 2005), pp. 3718–3720.
[48] The straight section after one MBA arc is shared by the short-pulse kicker and an insertion device. The short-pulse kicker is divided into two sectors: one is installed at the upstream part of the straight section, the other at the downstream part. The insertion device is installed in between.
[49] M. Paraliev, M. Aiba, S. Dordevic, C. H. Gough, and A. Streun, Development of Fast and Super-fast Kicker System for SLS 2.0 Injection, in Proceedings of 12th International Particle Accelerator Conference, *IPAC-2021, Campinas, SP, Brazil* (JACoW, Geneva, Switzerland, 2021), pp. 2887–2892.
[50] T. Taniuchi *et al.*, DC septum magnet based on permanent magnet for next-generation light sources, Phys. Rev. Accel. Beams **23**, 012401 (2020).
[51] The cavity operation point we choose is rather conservative and can be more aggressive to further prolong the bunches.
[52] The topology in longitudinal phase space transforms from normal bucket to alpha bucket with increasing rf voltage, when the second-order momentum compaction factor is finite. With $|\alpha_1/\alpha_2| > \sqrt{3}\delta_0$, a normal bucket is found in phase space, whereas an alpha bucket appears with $|\alpha_1/\alpha_2| < \sqrt{3}\delta_0$, where α_1 and α_2 are the first- and second-order momentum compaction factors and δ_0 is the (undeformed) bucket height. The bucket becomes asymmetric when $|\alpha_1/\sqrt{3}\delta_0\alpha_2|$ approaches 1. This parameter is 2.50 in the present SLS and reduces to 1.54 in the SLS upgrade.
[53] M. Böge, Beam-based alignment of beam position monitors at SLS 2.0, in *Proceedings of 14th International Particle Accelerator Conference* (2023), MOPM015, https://www.ipac23.org/preproc/pdf/MOPM015.pdf.
[54] J. Safranek, Experimental determination of storage ring optics using orbit response measurements, Nucl. Instrum. Methods Phys. Res., Sect. A **388**, 27 (1997).
[55] M. Aiba, Commissioning, PSI internal note, Report No. SLS2-AM81-006, 2022, http://ados.web.psi.ch/SLS2/Notes/?C=M; O=D.
[56] H. Wiedemann, *Particle Accelerator Physics* (Springer, Cham, Switzerland, 2015).
[57] R. P. Walker, Undulator radiation brightness and coherence near the diffraction limit, Phys. Rev. Accel. Beams **22**, 050704 (2019).
[58] M. Hosaka, J. Yamazaki, T. Kinoshita, and H. Hama, Longitudinal beam dynamics on an Electron Storage Ring with negative momentum compaction factor, in *Proceedings of 1st Asian Particle Accelerator Conf., Tsukuba, Japan* (1998), 5D018, https://accelconf.web.cern.ch/a98/APAC98/5D018.PDF.
[59] C. Steier *et al.*, On-axis swap-out R&D for ALS-U, in *Proceedings of 8th International Particle Accelerator Conference, IPAC2017, Copenhagen, Denmark* (JACoW, Geneva, Switzerland, 2017), pp. 263–265.
[60] P. Raimondi, private communication (2020).
[61] P. Raimondi, HMBA development, in *Proceedings of the 3rd Low Emittance Lattice design workshop* (2022), https://indico.cells.es/event/1072/contributions/1824/.